Dalton Transactions

Accepted Manuscript

ROYAL SOCIETY OF CHEMISTRY

www.rsc.org/dalton

Journal Name

ARTICLE

A Generalized Adsorption-Phase Transition Model to Describe Adsorption Rates in Flexible Metal Organic Framework RPM3-Zn

Received 00th January 20xx,
Accepted 00th January 20xx

DOI: 10.1039/x0xx00000x

www.rsc.org/

Angela D. Lueking,[a,b,†] Cheng-Yu Wang,[a‡] Sarmishtha Sircar,[a§] Christopher Malencia,[b] Hao Wang,[c] and Jing Li[c]

Flexible gate-opening metal organic frameworks (GO-MOFs) expand or contract to minimize the overall free energy of the system upon accommodation of an adsorbate. The thermodynamics of the GO process are well described by a number of models, but the kinetics of the process are relatively unexplored. A flexible GO-MOF, RPM3-Zn, exhibits a significant induction period for opening by N_2 and Ar at low temperatures, both above and below the GO pressure. A similar induction period is not observed for H_2 or O_2 at comparable pressures and temperatures, suggesting the rate of opening is strongly influenced by the gas-surface interaction rather than an external stress. The induction period leads to severe mass transfer limitations for adsorption and over-prediction of the gate-opening pressure. After review of a number of existing adsorption rate models, we find that none adequately describe the experimental rate data and similar timescales for diffusion and opening invalidate prior reaction-diffusion models. Statistically, the rate data is best described by a compressed exponential function, yet the resulting fitted parameters exceed the expectations for adsorption but fall within those expected for phase transition. By treating adsorption as a phase transition, we generalize the Avrami theory of phase transition kinetics to describe adsorption in both rigid and flexible hosts. The generalized theory is consistent with observed experimetnal trends relating to induciton period, temperature, pressure, and gas-substrate interaction.

Introduction

Study of adsorption into metal organic frameworks (MOFs), including those which exhibit a gate-opening (GO) phenomenon, has seen significant interest due to their potential in a variety of applications.[1] GO-MOFs typically have unique adsorption-desorption isotherms, typified by a sharp discontinuity at a particular adsorption pressure leading to an unusual S-shape, a large adsorption-desorption hysteresis, and a similar large discontinuity in the desorption branch. These isotherms have been described by the superposition of the isotherms of a first 'closed' structure and a second 'open' structure.[2] A review of the thermodynamics of the GO transition[3-9] as well as the history dependence of the closely related breathing materials[10] have been discussed elsewhere. Although *in situ* characterization techniques have demonstrated structural transformations in GO-MOFs,[11-18] very few of the *in situ* measurements are collected with the spatial and/or temporal resolution to monitor the kinetics of the GO transition. One exception is the use of X-ray grazing incidence diffraction techniques, which suggest the GO transition occurs at the particle edge, with guest molecules leading to shear, and co-existence of two crystalline structures.[19] To utilize GO-MOFs for gas separation and/or storage, it is important to understand how these structural transitions dictate the rate of gas adsorption.

RPM3-Zn, i.e. $Zn_2(bpdc)_2(bpee)$ [(bpdc = 4,4'-biphenyldicarboxylate; bpee = 1,2-bipyridylethene)], is a porous GO-MOF containing one-dimensional open channels with pore dimensions of ~ 5 X 7 Å (Figure 1). RPM3-Zn is highly flexible, and shows structural expansion/contraction upon guest inclusion/removal.[20] The flexibility arises due to the flexibility of the ligands.[14] We recently reported severe mass transfer limitations for low-temperature (77 and 87K) adsorption of H_2, N_2, and Ar to RPM3-Zn: adsorption uptake was strongly dependent upon the time allowed for equilibration of adsorption, and indirectly influenced by subtle equipment settings.[21] N_2 adsorption, in particular, increased twenty-fold when the allowed experimental time was increased to over 60 hours per data point.[21] The mass transfer limitations were much less pronounced for Ar and H_2, but yet, the adsorption isotherms were quite different: Ar exhibited an S-shaped isotherm while H_2 exhibited a typical Langmuir isotherm. We speculated that the S-shaped GO adsorption isotherm could be accounted for by a hypothetical two-regime activated diffusion model, in which diffusion is slow at low loading and rapid at high loading, corresponding to mass transfer limitations associated

---

[a] Department of Energy & Mineral Engineering and EMS Energy Institute, The Pennsylvania State University
[b] Department of Chemical Engineering, The Pennsylvania State University
[c] Department of Chemistry and Chemical Biology, Rutgers University, Piscataway, NJ 08854, USA
† Corresponding author. 120 Hosler, University Park, Pennsylvania 16802, USA. adl11@psu.edu, 814-876-0005

Electronic Supplementary Information (ESI) available: [Additional characterization data, Full model derivation, additional data with fitting]. See DOI: 10.1039/x0xx00000x with gas diffusion into two crystalline structures with very different pore sizes.[21]

Although two distinct rates of diffusion could possibly correspond to closed and opened structures, respectively, this constraint is not absolutely necessary. Diffusion limitations during adsorption usually become pronounced in porous materials as the size of the diffusing species approaches that of the pore, and are described by two regimes: in the Knudsen diffusion regime, the pore size is on the order of the mean free path,[22] whereas in the activated configurational diffusion regime the pore size is on the order of the molecular diameter.[23] As gas-surface potential, pore size, window size, and adsorbate size all influence the rate of diffusion, one would anticipate that the rate of diffusion would be dependent upon whether a GO-MOF structure was 'open' or 'closed'. However, even for configurational diffusion in rigid structures, the diffusing species must overcome the gas-surface potential to "hop" to the next site, and concentration dependence arises as a natural consequence of steric hindrance between diffusing species,[23] as demonstrated both theoretically[24, 25] and experimentally.[21, 26-28] In extreme cases, configurational diffusion in molecular sieves may be single-file or occur in clusters.[29] Past attempts to describe adsorption kinetics of MOFs include MD simulations[24, 25, 30] and gas-adsorption experiments.[27, 31] However, the lack of rigorous kinetics studies and models for adsorption in GO-MOFs, makes any generalizations difficult. Therefore, it is unclear as to whether diffusion in GO-MOFs is activated, is pressure or temperature dependent, and/or depends on MOF structure versus size of the diffusing species.

In this paper, we further explore experimental mass transfer limitations that arise for low temperature adsorption to RPM3-Zn. We utilize low temperature and pressure conditions such that the rate of GO and diffusion occur on similar time scales, and are experimentally observable via common adsorption techniques. Natural variations in particle size that arise due to subtle variations in synthesis are overcome by normalization of the rate curves by parameters obtained from the adsorption isotherms. We observe an unusual and pronounced induction period for adsorption for certain gases that leads to a sigmoidal rate curve. The induction period becomes more pronounced as we near the GO pressure (P_{GO}). We explore how common kinetic models, both from adsorption and other fields (catalysis, polymers, biological growth, phase transitions) can describe the rate data, and develop a generalized theory of adsorption/phase transition kinetics. The strong effect of adsorbate and temperature on the induction period and the rate of adsorption will likely have important ramifications for how these materials are used in large scale gas storage/separation processes.

Theory

Rates of adsorption are described as the progress towards equilibrium (θ) versus time (t). The progress towards equilibrium is the fractional change in the amount adsorbed relative to the equilibrium amount:

$$\theta = (M_t(t) - M')/(M_\infty - M') \rightarrow M_t(t)/M_\infty \qquad (1)$$

Where $M_t(t)$ is the cumulative mass adsorbed in the particle at any time, M' is the initial amount adsorbed, and M_∞ is the equilibrium uptake and thus a function of both temperature and pressure. For the rate data considered below, all adsorption steps are initiated from vacuum, thus M'goes to zero as noted in the secondary expression of (1) above. For GO-MOFs, $M_t(t)$ is comprised of mass adsorbed in both the closed ($M_c(t)$) and open $\left(M_o(t)\right)$ phases:

$$\theta = \left(M_c(t) + M_o(t)\right)/M_\infty = (\rho_c V_c + \rho_o V_o)/\left(\rho_c V_{c,\infty} + \rho_o V_{o,\infty}\right) \qquad (2)$$

Where the mass density of the adsorbate in the closed (ρ_c) and open (ρ_o) regions is also a function of temperature and pressure.

To tie the above expression to the models that describe phase transition kinetics, a relationship between amount adsorbed and volume transformed is required. Below, we will show that the amount adsorbed in the closed phase is negligible, such that $\rho_c \rightarrow 0$. In this limit, the fractional amount adsorbed reflects the volume transformed to the open phase:

$$\theta_{\rho_c \rightarrow 0} = V_o(t)/V_{o,\infty} = \theta_V \qquad (3)$$

Review of Common Kinetic Models

To describe the unusual rate behaviour of adsorption to RPM3-Zn, a number of rate models from various fields were considered. A brief review of these models is provided, with model numbers labelled with their abbreviation to differentiate the models from the other equations. All rate constants in the models have units of s^{-1}, unless otherwise specified.

Models of Fickian Diffusion. Fick's first law states that the diffusive mass flux is driven by a concentration gradient. Application of Fick's laws to adsorption in a porous material requires assumptions regarding the geometry and boundary conditions of the porous material. The micropore diffusion (MPD) model, derived elsewhere,[32, 33 21, 31, 34] is the solution to Fick's laws for spherical adsorbents, neglecting pore geometry and particle heterogeneity:

$$\theta = 1 - {}^{6}/_{\pi} \sum_{n=1}^{\infty} e^{-(n\pi)^2 k^o t}/n^2 \qquad \text{(MPD)}$$

The primary mass transfer coefficient derived from the MPD model, k^o, is the ratio of the rate of the effective intraparticle diffusivity (D) to the characteristic length of diffusion (L) squared, i.e. $k^o = D/L^2$. The effective diffusivity takes into account porosity and tortuosity of the adsorbent.[22] The length is the particle diameter, either calculated (e.g., total volume divided by external surface area[35]) or held constant.[36] Below, we opt for the latter approach by collecting sequential measurements.

As the geometry of porous adsorbents is often much more complex, more complex models extend this treatment. For example, the combined barrier resistance-diffusion (CBRD) model[36, 37] includes a secondary barrier to diffusion around the homogenous spherical particle, thereby introducing an exterior layer to the spherical particle that has a different diffusivity. Similarly, the dual diffusion resistance (DDR) model[38] assumes that secondary regions with different diffusivity are dispersed throughout the primary spherical geometry. One might envision these two models as "shrinking core" (CBRD) and "plum pudding" (DDR) geometries. The DDR and CBRD models lead to qualitatively similar trends as the MPD, i.e. a rapid initial uptake followed by a slower approach to equilibrium in the second region. Thus, the DDR and CBRD models are not considered in fits of the sigmoidal data below.

Semi-Empirical Rate Models. Diffusion may be described by an empirical power law (PL) expression[39, 40] at short time:

$$\theta = kt^n \qquad \text{(PL)}$$

As a general rule of thumb, if the initial rate of gas uptake is linear with √t (i.e. n=0.5), the rate of gas uptake is considered to be Fickian. If the rate of transformation is linear with time (n=1), this is considered "Case II". Intermediate values are considered to be anomalous diffusion, and values exceeding 1 are "Super Case II".[41, 42]

The LDF model can be derived by a mass balance between the gas versus adsorbed phases as adsorption occurs,[37] or via treatment of diffusion with a mass transfer coefficient and linear gradient:[34]

$$\theta = 1 - e^{-kt} \qquad \text{(LDF)}$$

The resulting decay rate, *k,* is related to k^o for spherical adsorbents as follows: $k^o = kL\alpha/6(1+\alpha)$, where α is the ratio of the pore to solid volume divided by the equilibrium partitioning coefficient between the two phases.[37] The LDF model predicts linearity on a semi-log scale. Experimental adsorption rate data that is better fit by the LDF model has been interpreted as an indication of surface, configurational, or activated diffusion rather than free (or Knudsen) diffusion along the pore.[36, 40]

The Double Exponential (DE) model[43, 44] is applicable when there are two mass transfer regimes, e.g. rapid diffusion into large feeder pores followed by slower diffusion into smaller branching pores:

$$\theta = A_1(1 - e^{-k_1 t}) + A_2(1 - e^{-k_2 t}) \qquad \text{(DE)}$$

Where the two regimes are weighted by a fractional contribution (A_1 and A_2), that is often assumed.

The Stretched Exponential mathematical function:

$$\theta = 1 - e^{-(kt)^{\lambda}} \qquad \text{(SE/CE)}$$

Has been applied to adsorption, with the stretching exponent or shape parameter (λ) interpreted as different molecular environments associated with multiple mass transfer regimes.[26-28, 45] This interpretation is consistent with the mathematical derivation of the SE as a weighted superposition of exponential decays, with the weighting parameter (λ) associated with a probability distribution function of the different relaxations.[46, 47] The shape parameter in the SE model is expected to be between 0 and 1,[47-49] which stems from the actual 'stretching' effect seen on the resulting rate curve about *kt*=1 (See Figure S1, Supporting Information). The SE is also commonly used to describe dielectric relaxation in polymers[50] and super-cooled liquids,[46] among other disordered materials.[51]

When the shape parameter (λ) exceeds unity, one arrives at a 'compressed' exponential (CE) about *kt*=1 (See Figure S1, Supporting Information), leading to a sigmoidal S-shaped response curve. A CE response arises when the characteristic relaxation time (i.e. k^{-1}) increases as the transition occurs, in other words, the process speeds up with the transition. Whereas the SE function arises from a continuous sum of exponential decays, the CE arises from a continuous sum of Gaussian functions.[52]

Note that the LDF, SE, and CE functions are all described by the same general equation, with different regimes of the shape parameter, i.e. λ=1, <1, and >1, respectively. A linear transformation (i.e. ln[ln [1/(1-θ)]] versus ln t) will yield the shape parameter as the slope of the transformed data.

Reaction-Diffusion Models. Tanaka et al.[53] developed a widely cited GO-Kinetic (GO-K) model to describe adsorptive uptake in GO-MOFs:

$$\theta = A_1\left(k_{go}e^{-k_{d1}t} - k_{d1}e^{-k_{go}t}\right)/\left(k_{go} - k_{d1}\right) + A_2\left(k_{go}e^{-k_{d2}t} - k_{d2}e^{-k_{go}t}\right)/\left(k_{go} - k_{d2}\right) \qquad \text{(GO-K)}$$

This model treats adsorption as a three step process: (1) Adsorption occurs to the crystal exterior; (2) A first-order "reaction" occurs to open the structure (with a rate constant k_{go}); and (3) Gas diffuses into the open structure. The authors combined processes (1) and (2) in the model, thereby presuming transformation preceded any intraparticle diffusion, and treating these processes as separable. This ignores any molecular-level interaction between the gas and the GO-MOF structure to initiate transformation. Diffusion (process 3) was treated via the two-barrier DE model with an assumed weighting between the two regimes.

We also considered a number of other reaction-diffusion models from both the polymer and catalysis literature. Like the GO-K, these models generally treat reaction and diffusion as separable to arrive at an analytical solution. Examples include the "shrinking" core model[54-56] and the "progressive conversion" model. [41, 54] In the former, reaction is fast relative to reaction. In the latter, the ratio is reversed, and the reaction is geometrically dispersed throughout the medium. Assumptions of a rate limiting step are often invalidated by transformations that alter the relative rates.[32, 33, 57-60]

In line with the GO-Kinetic model, we also consider a simpler 'Propagating Diffusion' (PD) model:

$$\theta = (1-e^{-k_{go}t})(1-e^{-k_1 t})+e^{-k_{go}t}(1-e^{-k_2 t}) \qquad \text{(PD)}$$

Like the GO-Kinetic model, bimodal diffusion is assumed with a first order transition (k_{go}) from the closed to open structure. Rather than assuming a fixed distribution between the two regimes and a three-step sequential process, the PD model simply allows for conversion from one regime to another with time, as might be expect from closed pores transforming to open pores.

Gompertz Growth Model. The Gompertz nested exponential function[61-64] is used to describe growth in an environment with limited resources:

$$\theta = e^{-\alpha e^{-kt}} \qquad \text{(Gompertz)}$$

With$\alpha = \beta/k$, and β is the rate of transformation under non-constrained conditions, and k is the decay in the growth rate due to nutrient limitations. The cumulative volume of the GO-MOF transformed to the open phase may also be limited to diffusion to the interface (illustrated in Figure S2, Supporting Information). Derived for the GO transformation (Section III of the Supporting Information), the parameters of the Gompertz function can be loosely interpreted as the inherent rate of transformation from the closed to open phase when at short time when there are no diffusion limitations *(β)*, and the rate at which this growth decays (k) due to increasing diffusion limitations at long time. As the Gompertz treatment presupposes an initial population or 'seed' required to initiate growth, this may be interpreted as the crystal exterior exposed to gas at the initiation of the adsorption experiment.

Avrami Kinetics of Phase Transitions. The CE function (λ>1) is often treated empirically, however, Avrami derived this expression in his treatment of the kinetics of phase transitions.[65, 66] Avrami first assumed the initial number of germ nuclei (N_o) was fixed only by the degree of departure from thermodynamic equilibrium (e.g. the degree of superheating or subcooling above the phase transition temperature), i.e.:

$$N_o = f(\mu - \mu^*) \qquad (4)$$

Where μ is chemical potential and μ^* is the potential at which phase transition is expected via thermodynamic considerations.

In Avrami's general treatment,[65] the rate at which germ nuclei (N) transform to growth nuclei (N') is given by:

$$\frac{dN'}{dt} = \dot{N}' = pN \qquad (5)$$

Where p is the probability of this transformation, which Avrami treated with an Arrhenius-like expression:

$$p = Ke^{-[E_A + A(\mu)]/RT} \qquad (6)$$

Where K is a proportionality constant, E_A is an activation energy for the phase transition, and A is the work required for the transition, T is Temperature, and R is the gas constant. The work term is anticipated to show complex temperature-dependence, levelling off to a near constant value at low temperatures (see, e.g. Figure 2 of [65]).

Although the specific mechanism for this transformation was originally unspecified, Avrami subsequently[66] differentiated germ versus growth nuclei by size. Growth nuclei had overcome a critical size to maintain steady growth, whereas germ nuclei were unstable due to the high interfacial energy required to nucleate a new phase. Indeed, it is the interfacial energy penalty required to nucleate the new phase that leads to a delay in nucleation, even when the bulk free energy of the new phase is thermodynamically more stable.

The number of germ nuclei (N) and growth nuclei (N') are given[64, 65] by:

$$N(t) = N_o e^{-pt}[1 - \theta_V(t)] \qquad (7)$$
$$N'(t) = N_o \int_0^t e^{-pz} [1 - \theta_V(z) dz] \qquad (8)$$

Where θ_V (defined by (3)) is a functional of N. These equations cannot be solved without assuming a geometric distribution of the nucleation sites.[65, 66]

To arrive at a general analytical expression, Avrami considered two-limiting cases for randomly dispersed nucleation sites: (A) the number of germ nuclei is very large and the probability of conversion is very low, such that the rate of nucleation is a constant; and (B) there is a high probability of transformation, such that there is an exponential conversion of germ nuclei to growth nuclei with time, i.e.:

$$\dot{N}' = pN \sim pN_o \sim constant \qquad (9A)$$
$$\dot{N}' = N_o e^{-pt} \qquad (9B)$$

In the former case, the number of large germ nuclei remains relatively unchanged over the course of the transformation, and N_o has been substitute for N to facilitate development of a generalized expression below.

At short time, the fractional volume converted to the new phase is:

$$\theta_{V,t\to 0} = \int_{\tau=0}^{t} \sigma \dot{N}' G^n (t-\tau)^n d\tau \qquad (10)$$

Where σ is a shape parameter (e.g. 4π/3 for a sphere), G is the linear rate of growth of a dimension of the new phase, n is the dimensionality of growth (with n=1 for one-dimensional, etc.), and τ is the induction period that is related to the probabilistic treatment of germ to growth nuclei conversion. When diffusion limitations are important, the growth rate is often observed to be proportional to square root of time, such that Equation (10) becomes:

$$\theta_{V,t\to 0} = \int_{\tau=0}^{t} \sigma \dot{N}' D^{n/2} (t-\tau)^{n/2} d\tau \qquad (10\text{-D})$$

Where G=dL/d($t^{0.5}$)=$D^{0.5}$ has been incorporated, as this follows from solutions to Fick's Law.[22]

The second primary assumption in Avrami's development is that there is cessation of growth when adjacent regions collide, which is not accounted for in Equation (10). With a probabilistic geometric argument on how to exclude the overlapping regions, Avrami arrived at:

$$\theta_V = 1 - Exp[-\theta_{V,t\to 0}] \qquad (11)$$

A common assumption is constant isotropic growth, leading to:

$$\theta_{V,AR} = 1 - Exp[-\sigma p N_o G t^2/2] \qquad (12\text{-A})$$
$$\theta_{V,BR} = 1 - Exp[-p\sigma N_o G(-1 + \mathrm{e}^{-t} + t)]$$
$$\sim 1 - Exp[\,-p\sigma N_o G t] \qquad (12\text{-B})$$
$$\theta_{V,AD} = 1 - Exp[-2\sigma p N_o D^{0.5} t^{1.5}/3] \qquad (12\text{-AD})$$

Where one-dimensional growth has been assumed for brevity and the labels refer to the limiting cases noted above and "D" denotes to diffusion control. Equation (12) is thus the CE function, with the time exponent reflective of the dimensionality of growth, the role of diffusion, and the nucleation regime. Thus, it is common in the field to differentiate between homogenous nucleation (Case (A)) and heterogeneous nucleation (Case (B)), where the former augments the exponent by one. One will note from Equation (12) the general form of the CE rate constant:

$$k_{CE} = ap(T, \mu_{ads}, D) N_o (\mu - \mu *) G^n(T) \qquad (13)$$

When nucleation of the new phase is diffusion-limited, G^n is replaced by$D^{n/2}$.

Application of Avrami's Development to Adsorption. To reapply Avrami's development to adsorption, we consider the phase transition to be from a closed state with no adsorbate to an open state with an adsorbed film. Whereas Avrami growth presumes the geometry of the growth phase is outward from a number of seeds dispersed through the first phase, we presume growth is in the opposite direction, i.e. it occurs inwards from the surface of the particle. Similar to the MPD development, we assume a spherical particle of homogenous composition, such that the resulting mass transfer coefficient will be related to an "effective" diffusivity. In this geometry, the new growing phase will be an annulus at the periphery of a sphere. A full derivation is provided in Section II of the Supporting Information. We arrive at the following expressions when we presume growth rate to be proportional to $t^{0.5}$ and t^1 (for diffusion versus reaction control), respectively:

$$\theta_{V1/2} = 1 - (1 - k^{0.5} t^{0.5})^3 \sim 1 - e^{-kt^{0.5}} \qquad (14)$$
$$\theta_{V1} = 1 - (1 - k't)^3 \sim 1 - e^{-kt} \qquad (15)$$

For a cylindrical particle, when edge effects are ignored, when the growth rate is proportional to $t^{0.5}$ and t^1, respectively:

$$\theta_{V1/2} = 1 - (1 - k^{0.5} t^{0.5})^2 \sim 1 - e^{-kt^{0.5}} \qquad (16)$$
$$\theta_{V1} = 1 - (1 - k't)^2 \sim 1 - e^{-kt} \qquad (17)$$

In each case (Equation 14-17), the final approximation is true for small *kt* (See Supporting Information). Thus, adsorption to the exterior of a single spherical or cylindrical particle, with progression inwards, will lead to apparent shape parameters of ½ and 1, respectively. If rather than a single spherical or cylindrical, there is a number of spheres of equal size, the result is unaltered. Edge effects for a cylindrical particle and a distribution of particle sizes can be expected to alter the exponent.

If, rather than considering adsorption to the exterior of a single spherical or cylindrical particle, we allow for several growing regions, each with a certain probabilistic induction period for growth, and discount overlap according to Equation 11, we arrive at:

$$\theta_{VD} = 1 - Exp\left[-\theta_{\frac{V1}{2}}\right] \sim 1 - Exp[-k^{1.5} t^{1.5}] \qquad (18)$$
$$\theta_{VL} = 1 - Exp[-\theta_{V1}] \sim 1 - Exp[-(k't)^3] \qquad (19)$$

The effective shape parameters are 3/2 and 3 for one-dimensional growth. Due to the integration, shape parameters less than unity are not possible in this geometry for any dimensional growth and any assumption of time dependence.

Methods

Materials. Two separate batches of RPM3-Zn, subsequently referred to as "i" and "ii", were both synthesized according to published procedures, as outlined previously [21]. Single crystal X-ray diffraction studies revealed that RPM3-Zn is a microporous structure with a 3D network containing parallelogram shaped 1D channels with solvent accessible volume of 1171.9 Ǻ (27.6% of the unit cell volume 4243.4 A^3).[3 20] Powder X-Ray diffraction (PXRD) of both batches matched the single crystal data (Figure S3, Supporting Information). Elsewhere, PXRD demonstrated reversible distortion of the lattice after solvent removal under mild conditions.[20] No attempt was made to vary the resulting particles, but natural variations in methodology led to subtle differences in the particle size and quality of the two batches. Thus the two samples provided an opportunity to explore the effect of small variations of crystal/particle size on the rate of uptake. Optical microscopy of about 50 images demonstrated both batches were comprised of rod-shaped particles, with slight variations in length: 40-60 µm for Batch i and 50-70 µm for Batch ii (Representative images shown in Figure S4, Supporting Information).

Adsorption Measurements. Adsorption of ultra-high purity grade gases (99.999%) to the Batch i powder was collected on a commercial volumetric unit (ASAP 2020, Micromeritics) using 113 mg of sample. The powder was outgassed at high vacuum (~5 x 10^{-3} mmHg) at 135^{o}C for at least eight hours prior to measurement of the isotherm. The temperature was maintained using a bath of liquid nitrogen (77K) or liquid argon (87K), which was replenished every 48 hours for long experiments. The adsorptive temperature was calculated from an automatic measurement of the saturation pressure (P_o) for N_2 at 77 K while for N_2 at 87 K, bath temperature is entered manually and P_o is calculated from a standard table. The ASAP determines measurement time based on checks of pressure stability at fixed time intervals, until the relative pressure reading is within 0.01% of the absolute pressure. The time between stability checks (*dt*) was altered as a means to increase the equilibration time from *dt*=5 to *dt*=360 seconds for N_2 at 77K to *dt*=90 for 87K measurements. The minimum time is 11*dt*, and the maximum time exceeded 10^5 seconds. All rate data was collected after a single pressure increase from a fully evacuated sample, and pressures were chosen above and below the GO pressure reported in the previous publication.[21] Pressure data were collected manually and validated against standard measurements at various times and pressures. Blank tube experiments in He confirmed pressure were within manufacturer specifications for pressure stability (i.e. < 0.0007 mmHg/min) over the time scale of a typical experiment (i.e. ~28 hours). The pressure variations observed in these blank experiments corresponded to negligible apparent adsorption when the data was converted to moles adsorbed assuming a typical sample mass (see Figure S5a in Supporting Information). Small, but non-negligible leak rates do exacerbate the error bar for long time volumetric experiments (e.g., the measured lead rate over 100 hour leads to an error bar of ~7 cc (STP)/g for a 70 mg sample). However, leakage in sub-ambient pressure experiments tends to under estimate adsorption, and thus the observed slow adsorption rates cannot be attributed to leakage.

Additional gas (99.999% purity) adsorption measurements to Batch ii were collected using a thermogravimetric analyzer (Hiden IGA-001) at either 77 K or 87 K using 47 mg of sample. The gas (N_2, Ar, or H_2) was charged at a ramp rate of 100 mbar/min to the desired pressure, and the data during this initial ramp period (typically a few minutes or less) was discarded due to turbulence in the system leading to erratic weight readings. Buoyancy corrections were based on measurements of sample gas density in He at 300K. The liquid in the cryo-bath was refilled ever twelve hours which led to minor inflections in the rate data. The measurement was maintained until the mass stabilized at $<10^{-4}$ mg/min. A sequential test on the same batch of sample verified the uptake was equivalent on the two pieces of experimental equipment (Figure S5b, Supporting Information).

To account for differences in inherent diffusivity and particle size, all adsorption measurements for a given batch were collected sequentially to maintain constant particle size (and hence characteristic diffusion length) for a given batch. In an attempt to eliminate history dependence, all adsorption rate data were collected from vacuum on a freshly evacuated sample. Yet, the two batches of RPM3-Zn inevitably had different particle size (Figures S4, Supporting Information) and structural perfection and defects, both of which are expected to alter the mass transfer coefficient (see, e.g. Figure S8, Supporting Information). We noted that the rate curves followed predictable pressure trends when the pressure was normalized by the corresponding P_{GO}, as determined by the adsorption isotherm, and thus used this methodology to compare the two batches.

Numeric Treatment. Experimental rate data was converted to fractional uptake by dividing by the truncated maximum uptake that was experimentally determined at the longest collected time. Data was collected until the weight change was within the sensitivity of the instrument ($<10^{-4}$ mg/min, as determined previously [67] and verified with a blank experiment) for about eight hours (see, e.g. Figure S6, Supporting Information). In many of the figures below, an eight hour stability period may appear truncated, but this is due to the very long time scale of the experiments, which were often on the order of weeks. The effect of this stability criteria, i.e. the length of time in which adsorption had reached the saturation value, had little effect on the parameters obtained in the data fits (Figure S7, Table S1, Supporting Information). Data fitting was performed by minimizing the sum of least squares of the residues in a commercial software package. In the fits, all data was weighted equally on a linear time scale. Although fitting the data on a logarithmic time scale may provide a better fit of short time data, this is generally necessary only when there is a steep rise at short time, followed by the majority of the data collected at near saturation [47], which was not the case in the rate data presented herein. The initial guesses of the fitting parameters were varied on several iterations to arrive at the best data fit. Data fits to the stretched exponential model were conducted by first constraining the shape parameter (λ) to be <1, and then fitting the data without constraints. From these fits, the correlation coefficient (R^2), residue of fitting (i.e. the difference between model fit and the experiment), Akaike information criterion (AIC), and Bayesian information criterion (BIC) parameters were computed.

We also consider adsorption of N_2, Ar and O_2 to Cd(bpndc)(bpy) (1; bpndc=benzophenone-4,4'-dicarboxylate, bpy=4,4'-bipyridyl) at 90 K using digitized kinetic rate data, previously collected by dosing to a fixed pressure on a volumetric apparatus.[53]

Results and Discussion

Adsorption Isotherms and Mass Transfer Limitations

The 77K N_2 adsorption isotherm of the two batches had differences in both capacity and the P_{GO} (Figure 2a, upper curves), which can be attributed to either slight differences in crystallinity (Figure S3, Supporting Information) or particle size (Figure S4, Supporting Information), despite identical synthesis procedures. The potential effect of crystallinity on capacity is clear, as a structured pore affects the volume available for adsorption as well as the gas-surface interaction. The potential effect of particle size on adsorption isotherms is unexpected, unless one considers very slow adsorption rates with an allowed experimental time that does not allow for full thermodynamic equilibration. As shown previously[21] and in the following section, Ar adsorption at 87 K is significantly faster than N_2 adsorption at either 77 or 87 K. The saturation capacity of these two materials converge for Ar at 87 K (Figure 2C), yet diverge for N_2 at both 77 and 87 K (Figure 2A and B, respectively). It thus seems likely the differences in N_2 capacity can be attributed to kinetic effects and particle size.

The rod-like particles of Batch ii were slightly larger than Batch i (~40-60 µm for Batch i and ~50-70 µm for Batch ii; see Figure S4, Supporting Information). With larger particles, the rate of mass transfer to Batch ii will be more subject to mass transfer effects, as particle size will affect the overall mass transfer coefficient (*k*), which is defined as the gas diffusivity (*D*) within the material divided by the characteristic diffusion length (*L*) squared (i.e. $k=D/L^2$)[22]. For constant diffusivity, the effect of particle size is pronounced, due to the squared dependence of characteristic diffusion length, as illustrated further in Figure S8 (Supporting Information). Although observed differences in the external length of the rod-shaped particles was small, the characteristic diffusion length would also depend upon the distribution of particle sizes, the crystallinity, the length to width ratio of the rods, the presence of defects, dislocations, etc. These differences are manifest in the adsorption isotherms of the species, and are particularly pronounced for species with very slow adsorption rates such as N_2.

Likewise, the influence of material variation on P_{GO} shows several anomalies: At 77 K, P_{GO} was higher for batch i, whereas at 87 K, P_{GO} was higher for batch ii for both N_2 (Figure 2B) and Ar (Figure 2C) isotherms. As the number of pressure points in the isotherms of the two materials was not held constant, one will note that for N_2, an increased number of low pressure points below the apparent P_{GO} tends to decrease the $P_{GO.}$ An increased number of pressure points effectively increases the allowed time for slow diffusion to occur, and thus decrease the $P_{GO.}$ However, it is likely that none of these isotherm points reach true equilibration.

The opposite trend is observed for Ar 87 K adsorption: Batch ii has an increased number of pressure points below the P_{GO}, but an increased P_{GO} relative to Batch i. This is unlikely to be attributed to thermodynamics or sample quality, as the opposite trends in P_{GO} were observed for N_2 at 77K. Thus mass transfer limitations may lead to anomalous adsorption isotherms even for "rapid" adsorption of Ar at 87 K, particularly as the rate of adsorption slows at pressures near P_{GO} (as will be shown below). Some papers in the field have noted "history effects" for adsorption isotherms of GO-MOFs. Here, the apparent "history effects" are really mass transfer effects combined with insufficient time for true thermodynamic equilibration.

Further, severe mass transfer limitations for both Batch i and ii are easily demonstrated by varying the frequency with which the equipment assesses pressure stability, as discussed fully in our previous publication.[21] In brief, we can alter both the adsorption capacity and the extent of hysteresis by varying the experimental time parameters used by the equipment to assess stability. The difference between the upper and lower curves in Figure 2a is the frequency with which the automated procedure checks for pressure stability (e.g. less than 0.01% pressure variation, which is the default for the equipment), thereby signally adsorption is complete and initiating the next step in the adsorption isotherm. For materials that exhibit Fickian-diffusion, adsorption rates are initially rapid and then slow as the driving force for adsorption is decreased. In this scenario, the standard criteria by which to establish equilibration is quite rigorous, and will be relatively independent of the frequency of the stability checks. However, this standard criteria will be insufficient when the rate of adsorption is first slow, and then accelerates, which is the type of behaviour observed for low pressure and temperature measurements of RPM3-Zn, as discussed in the next section. In this scenario, the system may meet the stability criteria during the initial slow period. This was the case for the lower curves of Figure 2a, in which we used a rapid frequency (5 seconds) to check for stability. Adsorption is completely missed, as the minimum allowed time (after eleven stability checks, or approximately one minute) does not exceed the initially slow induction period. The lack of adsorption for the lower curves justifies our assumption that the adsorbed-phase density in the closed phase approaches zero (i.e. Equation 3). The frequency with which stability was assessed for the upper curves of Figure 2a was increased to 60 seconds, and the minimum allowed time was sufficient to detect slow adsorption during the induction period. As this is a frequency for assessment rather than a fixed time, some points in the upper curve required over 60 hours *per data point* to satisfy the stability criteria, and the upper curves each required several weeks to complete. Even with such long equilibration times, it is not clear that these isotherms are at true thermodynamic equilibrium.

Thus, mass transfer limitations may lead to under-prediction of experimental adsorption isotherms, over-prediction of $P_{GO,}$ and apparent history effects. These mass transfer limitations will be exacerbated at low temperature. We also anticipate they may lead to additional experimental anomalies, some of which have been reported in the literature for GO-MOFs, including anti-Arrhenius behaviours and adsorption capacities that increase with increasing temperature. For this reason, we turned our attention to measurement of adsorption rates from single-step pressure increments from vacuum in subsequent sections to minimize history effects and mass transfer limitations.

Rates of Adsorption

General Observations and Trends. The N_2 adsorption rate curves collected at 77K (Figure 3) and 87 K (Figure 4) were very slow, particularly at pressures near or below the PGO. At the lowest pressure and temperature studied (i.e. P/PGO=0.8, 77 K, Figure 3), adsorption was incomplete after 10 days (i.e. 80 x 104 s). Slow adsorption rates at cryogenic temperatures are not unusual, as thermal energy may be insufficient to overcome barriers for activated (a.k.a. configurational) diffusion in micropores. However, two highly unusual features are noted in the rate data, including a clear acceleration of adsorption and an appreciable induction period for adsorption, most notably at 77K.

The acceleration of adsorption is most apparent after a transformation of data to a semi-log plot (Figure 3A' and 4A'), and is particularly pronounced at low temperatures and pressures, particularly at pressures below the PGO. Examination of similar semi-log plots for other adsorbents would typically show linearity over the majority of the plot, or a decrease in slope at long times.

All 77K N_2 adsorption rate curves exhibited sigmoidal rate behaviour, with an initial induction curve followed by a sharp increase in the adsorption rate. The induction period is clearly visible for the 77 K data at low pressure (Figure 3A). For example, batch i at P/P_{GO}=1.6 and ii at P/P_{GO}=3.0, there is very little adsorption until ~5x10^4 seconds (14 hours), after which the rate of adsorption abruptly increases. At higher pressures, the induction period is less visible due to a drastic change in the time scale. However, constructing an Avrami-like plot (Figure 3A" and 4A") shows a change in slope at approximately 1 hour (i.e. ln 3600 seconds ~ 8) for both 77 K and 87 K data, although it is much more pronounced in the former. One hour of data collection is well beyond the initial pressure increase for both the gravimetric and volumetric adsorption measurements, as this typically occurred on the order of minutes and seconds of data collection, respectively. The corresponding coverage at this infection point is very small, typically 1-3% of the final value, suggesting the gas adsorption is very low when the transition occurs. Some of the volumetric data that was collected manually lack this transition, likely due to insufficient resolution of the data collection. A change of slope in the Avrami consideration is indicative of a change in mechanism, as discussed further below.

At 77 K, no induction period was observed for either H_2 or O_2 at 77 K (Figure 5A). Argon behaved qualitatively similarly to N_2 when considered at comparable pressures (e.g. ~90 mbar, Figure 5A). The induction period for N_2 and Ar was similar (~4 x 10^4 seconds, at ~90 mbar and 77 K), and then Ar diffused more rapidly into the structure. In our previous publication [21], we also discussed the much slower uptake of N_2 relative to Ar, and stated that the effective frequency of Ar in the structure had to be four to five times greater than N_2 to account for the differences. Although mathematically true, this previous analysis was based on the characteristic time of adsorption taken from automated adsorption isotherms, and assumed diffusion to be Fickian, which is invalidated by the sigmoidal behaviour observed in the full rate curves as discussed further below. No pronounced induction period was observed for either N_2 or Ar with just a 10 K increase in temperature to 87 K (Figure 5), at any pressure studied (see also Figure 4).

Kinetic Model Selection. All experimental data was fit to all models (See Section IV of the Supporting Information). Our criteria to evaluate the efficacy of the various models to describe the data were three-fold: (a) provide a mathematical description to facilitate discussion; (b) find the model with the greatest applicability to fit all data; and (c) provide some mechanistic insight into the combined process of gate-opening and diffusion. In addition to the common R^2 parameter, we utilized the AIC statistical parameter (See Table S2, Supporting Information), which penalizes for the number of fitting parameters to defend against over fitting. The AIC statistical parameter is a widely-used approximation to the more theoretically-grounded Bayes Factor. A brief evaluation of the models follows.

Consideration of the short time data via the semi-empirical power-law expression demonstrates all gravimetric rate data falls within the "anomalous" regime, with the exponent ranging from 0.7-0.8 at 77K and 0.9-1.0 at 87 K (Figure S9). However, this consideration provides relatively little mechanistic insight and is valid only at short time.

Given the pronounced sigmoidal behaviour (Figure 3A), the 77 K data was poorly described by the common adsorption rate models such as the MPD, LDF, and SE models. The error residuals were as much as 20% at short time (Figure 3B) and the fitting parameters were poor relative to the other models (Table S2, Supporting Information). Mathematically, the LDF, DE, and SE functions cannot capture sigmoidal behaviour for any values of the fitting parameters. Similarly, the Fickian MPD, DDR, CBRD models cannot capture sigmoidal behaviour. At 87 K, without an appreciable induction period, both the LDF and SE models adequately described the data ($R^2 \geq 0.997$, see Table S3, Supporting Information and Table 1, respectively); the error residuals are highest at short time (Figure 4B). The MPD model remained a poor fit relative to the other models (R^2~0.97, Table S2) with high error residuals (Figure S11g). The AIC statistic suggested the added complexity of the SE model (relative to the LDF) was justified only at $P<P_{GO}$ (Table S2). For N_2 at 87 K, the SE mass transfer coefficient ranged from 1 to 10 x10^{-5} s^{-1} (Table 1). At comparable temperatures and pressures (i.e. ~90 mbar and 87 K, Figure 5), the SE mass transfer coefficients for N_2, Ar, and H_2 were 1.2, 7.3, and 40 x10^{-5} s^{-1}, respectively (Table 1). The LDF mass transfer coefficients were almost identical (Table S3A, Supporting Information).

It is worth noting that we were unable to fit the sigmoidal 77 K data to the GO-Kinetic model, which was specifically developed to describe adsorption rates in flexible GO-MOFs. In most cases, the fitted rates of reaction and diffusion were of equal magnitude (i.e. k_{go}~k_{d1}, see Table S3C, Supporting Information), which led to both division by zero in the model equation and invalided the assumption that diffusion and reaction were separable, as incorporated into model development. Similarly, we were unable to fit the sigmoidal 90 K N_2 rate data that was found in the paper that developed this model.[53] Although the logarithmic 90 K Ar and O_2 data were adequately described by the GO-Kinetic model, we also found the LDF model adequately described the data (Section V, Supporting Information). We thus did not consider the GO-Kinetic model further.

The PD model provided a better fit than the GO-Kinetic model and led to the best fitting statistics for the 87 K data (Table S2, Supporting Information). However, the fitted rate constant for opening (k_{go}) was pressure-dependent (Table S3D, Supporting Information), a feature also noted by Tanaka et al. in development of the GO-Kinetic model.[53] Dependence of the rate of transformation on the pressure external to the particle seems to imply a stress-induced transformation. However, we found that the rate of adsorption for different gases to be drastically different at comparable pressures (Figure 5), somewhat inconsistent with a stress-induced transformation and more indicative of a unique gas-substrate internal interaction that should be fairly independent of external pressure.

Elsewhere,[68] we explored fitting the data to other reaction-diffusion models, by assuming these two variables were separable, but we could not reproduce sigmoidal rate behaviour. This analysis is summarized briefly in Section VI of the Supporting Information.

The statistics of fits to the Gompertz growth model were quite good in most cases (Table S2, Supporting Information). Considering the resulting fits, the Gompertz ratio ($\alpha=\beta/k$) showed somewhat remarkable convergence for all data (Table S3E, Supporting Information). Specifically, at 77 K, α ranged from 2.8-4.4 for $P>P_{GO}$ data, and then increased to 6 for $P<P_{GO}$. At 87 K, the α parameter ranged from 2.1-2.8 for all N_2 data (at six pressures). Presuming α is related to the ratio of the rate of reaction (i.e. gate opening) to diffusion, as noted above, the decrease in α for the 10 K increment can be attributed to a more pronounced effect of temperature on reaction than on diffusion. At 87 K, α is 2.5 for Ar and 1.6 for H_2, relatively close to that seen for N_2, despite large apparent differences in the unprocessed rate curves (Figure 5). In all cases, the magnitude of the α parameter (i.e. <10) would suggest reaction and diffusion occur over similar time scales for all conditions considered (Table S3E), consistent with our conclusion after application of the reaction-diffusion models. Although this was a fairly satisfactory result, it provided no real insight into the trends of the various data sets, in particular, the trends in the gas-surface interaction.

In the end, the model with greatest applicability for all data was the SE/CE model, when the shape parameter was unconstrained, such that it was allowed to be either above or below unity. The SE/CE model had very low error residuals (Figure 3B, 4B), the best fitting statistics for the 77 K data, and the best statistics for the 87 K data when the invalidated reaction-diffusion models were excluded (Table S2, Supporting Information). The CE model was able to describe the sigmoidal adsorption rates when the rate of opening became significant, and as temperature was increased to 87 K, modification of the shape parameter was able to capture this data as well. Further interpretation of the shape parameter is provided in the Section “Revisiting and Extending Avrami Theory” below.

Trends for the combined SE/CE Model. To consider the SE/CE fits for all data, we have reapplied the “universal adsorption theory”,[69] which defines reduced adsorption potential as follows: $\mu_R = - RT/T_C \ln (P/P_C)$. In brief, this theory provides a theoretical framework to reduce various state variables by the critical parameters, similar to the corresponding states practice for considering gas compressibility. We previously demonstrate this treatment led to convergence of several experimentally determined thermodynamic adsorption properties of GO MOFs, allowing side-by-side comparison of both subcritical and supercritical adsorbates.[69] H_2 is expected to deviate from this treatment due to quantum effects,[69, 70] and thus the reduced chemical potential of H_2 has been (somewhat arbitrarily) divided by 10 here so that it may be plotted on the same scale as the other gases. Application of the universal adsorption theory here is intended only to provide a single independent variable that incorporates temperature, pressure, and adsorbate. Consideration of the full data set in this light (Figure 6) shows certain trends in the SE/CE fitted rate parameters that will be discussed in the next section.

The SE/CE model fits of the combined data set (Figure 6) show that for a given gas, the rate constants at 87 K are greater than 77 K, as expected. The rate constants also increase with increasing pressure, as expected. They also tend to cluster with molecular size, with oxygen and hydrogen having faster rates of adsorption than N_2 and Ar. This is consistent with conventional wisdom dealing with porous materials with molecular sieving behaviour. For example, a significantly increased O_2 diffusivity relative to N_2[71] and Ar[72] was observed for carbon-molecular sieves, which is generally attributed to a small difference in molecular size (for O_2-N_2) or molecular weight (Ar).

The shape parameter (λ) also shows interesting trends (Figure 6B). The H_2 value (0.58, Table 1) is close to that determined empirically for Fickian diffusion with an assumed particle size distribution (i.e. 0.65).[36] This implies H_2 diffuses freely (or in the Knudsen regime) through the pore, relatively uninfluenced by the surface potential. Excluding H_2, the shape parameter for the other gases at 87 K is close to 1 (i.e. $0.92 < \lambda < 1.2$, Table 1), suggesting the LDF model would provide an adequate fit. Indeed, the AIC statistic suggests the added parameter of the SE/CE model (relative to the LDF) is hardly justified for $P>P_{GO}$, although it is warranted at $P<P_{GO}$ (Table S2). Adsorption that follows the LDF function is commonly attributed to constrained (a.k.a. activation or configurational) diffusion through a surface potential.[36, 72] Yet, when the combined data set is considered (i.e. Figure 6B), the subtle variations of the shape parameter above/below 1 at 87 K appear to be more than a statistical aberration, as the CE function is clearly warranted for the 77 K data and much of the 77 K and 87 K data start to converge on the reduced scale of Figure 6B. Interestingly, the SE function (with $\lambda \leq 1$) is common to adsorption while the CE function (with $\lambda \geq 1$) is commonly applied to describe phase-transitions, with both regimes bounded by the LDF function (with $\lambda=1$). A possible explanation of the convergence of these two regimes is discussed in the “Avrami” section below.

At 77 K, the shape parameters of N_2 and Ar data tend to cluster between 1.5 and 2 when the full rate curve is fit to the SE/CE model. (One data point exceeds 2, yet was not likely fully equilibrated after the 190 hours that was allotted, leading to somewhat poor fits to the CE Model. See, e.g. Figure S3b, Supporting Information.) Notably, we can find no other cases in describing gas adsorption that lead to a shape parameter that exceeds 1. Indeed, a sigmoidal rate curve is inconsistent with the general premise of Fickian diffusion, in that the rate of mass transfer is proportional to the concentration gradient. Thus, the greatest rate of adsorption should occur at short time, regardless of the types of assumptions and boundary conditions that are incorporated into solution of Fick’s law.

Rather, a clear acceleration of adsorption implies a cooperative process, such that an early initiation step facilitates further adsorption. Given the flexibility of the framework, it is reasonable to conclude that early opening of the structure facilitates additional adsorption, either by increasing the diffusivity of the gas within the material or increasing the internal stress thereby initiating further opening. Notably, a sigmoidal response has been observed for gas-induced swelling of flexible amorphous polymers,[59, 60] coal,[73] glasses,[47, 49] as well as the dynamic response of disordered soft materials (e.g. colloids,[74-76] gels,[74, 75] clays,[77] polymer melts[76] etc.) and fluids confined in complex, heterogeneous, anisotropic media.[52] Such a delayed response has been attributed to cooperative motion of particles, relaxation of internal stresses,[77] and ballistic motion.[74] Much of the use of the CE function to describe the response is empirical, the exception seems to be Avrami's treatment of phase transition kinetics, which is explored further below.

Revisiting and Extending Avrami Theory

In an attempt to move beyond empiricism and explain some of the unexpected trends with temperature, pressure, and adsorbate, we reapplied Avrami's general treatment[65] (i.e. Equations 4-13) to the case of adsorption, as developed in Equations 14-19 above. Adsorption is considered to be a phase transition from a closed, empty pore to an adsorbed film in the host, regardless of whether creation of the film is accompanied by a significant change in pore volume.

Validation of Assumptions. The adsorption isotherms of Figure 2 validate the assumption that the fractional amount adsorbed is analogous to the fractional volume transformed (i.e. Equation 3). Large subsets of the data meet the criteria outlined by Avrami for 'isokinetic behaviour' (see Section VII of the Supporting Information). However, this is a somewhat inconclusive validation of the applicability of the Avrami treatment.

To further validate use of the generalized Avrami theory to describe adsorption, we consider adsorption to the exterior of a rigid cylindrical host, as noted in development of Equations 16-17 above. Creation of an annulus of the adsorbed film (i.e. the new phase) that proceeds inward is similar conceptually to the concentration "front" expected for Fickian diffusion. The effective shape parameters from Equations 16-17 fall within the "adsorption regime" (i.e. $\lambda < 1$). They are also approximately consistent from numerical data generated from the MPD (i.e. 0.65 from Ref.[36] with assumed particle size) and LDF (1) equations when fit to the SE/CE model. The results are qualitatively consistent with the experimental results of rates of adsorption to a rigid host, which are commonly described by the SE function with fitted values typically between 0.5 and 1. Justification of use of the SE function to describe adsorption kinetics has been somewhat qualitative, with arguments presented in the Theory section above.

When growth is distributed throughout the particle, rather than at the particle exterior, the effective shape parameters for our theoretical development (Equations 18-19) exceeds unity for any geometry, and with any assumed time dependence. Thus, it is the distribution of the growing regions throughout the particle that lead to an effective shape parameter exceeding unity, such that the resulting response curve is in the "phase transition" regime ($\lambda > 1$).

This suggests that the experimental data with a shape parameter far exceeding one (see Fig. 5B) result from phase nucleation of the new adsorbed phase throughout the particle rather than at the particle exterior. In other words, a shape parameter below unity is indicative of nucleation at the exterior with high probability. A shape parameter exceeding unity is indicative of delayed and probabilistic growth with nucleation sites dispersed throughout the particle. Avrami's general treatment[65] also noted the possibility of spatial variations, in particular, those arising due to grain boundaries. However, to arrive at a final analytical expression, spatial variations were ignored, and nucleation sites were assumed to be dispersed uniformly.[66] Similarly, we note diffusion limitations may also give rise to spatial variations in the probability of nucleation via the work term in Equation (6). Without a more quantitative treatment of spatial variations, the Avrami treatment is somewhat qualitative. Yet, it is able to consistently explain all observed trends in the data, as discussed in the following sections.

Induction period (Nitrogen). The induction period observed in the N_2 experimental data (Figure 3A) can easily be explained by Avrami's probabilistic treatment of phase nucleation (Equation 10). The length of the induction period is related to both the number of germ nuclei (Equation 4) and probability of nucleating the growth regions. The former is determined by the departure from thermodynamic equilibrium, whereas the latter is determined by temperature, proximity to a grain boundary that would lower nucleation of a growth phase, and local chemical potential, which would incorporate potential diffusion limitations. The effect of each of these external stimuli on the data is elaborated upon further below.

Effect of Pressure (Nitrogen). The probability of transformation from germ nuclei to growth nuclei is only a weak function of external pressure, showing up in the work term of Equation 6. (Note: Internal diffusivity is a function of a concentration gradient, not the external pressure.) An increased pressure would decrease the work for phase transition, leading to a slight increase in the probability of transformation. An increased external pressure represents an increased departure into the metastable region, thereby increasing the number of germ nuclei (Equation 4). Both an increased p and an increased N_o will increase the rate constant (Equation 13), consistent with what is observed (Table 1). A decrease in rate constant will decrease the "apparent" induction time. Indeed, when the data is normalized per a characteristic time (see Figure S16, Supporting Information), the short time data converge at a given temperature for all pressures measured. Thus, the pressure trends are consistent with the expected dependence of the rate constant on the probability and/or nucleation sites.

Effect of Temperature (Nitrogen). There is a notable shift in the shape of the N_2 rate curves between 77 K and 87 K. Visually, the 77 K data appears sigmoidal whereas the 87 K data appears logarithmic. Qualitatively, it is often stated that reaction rates have a much stronger temperature dependence than diffusion rates. Presuming only a minor change in diffusivity within a 10K increment, a significant decrease in the probability of nucleation (i.e. opening) would have a large effect on the rate-limiting step. Thus, although there is less thermodynamic incentive for adsorption at 87 K than 77 K (Figure 2), there is greater thermal energy to facilitate the phase transition at 87 K, thereby increasing the probability of nucleation/opening, and leading to a larger pore structure for more rapid subsequent diffusion. An abrupt shift in the rate-limiting-step is thus qualitatively consistent with the probability of phase nucleation having a strong temperature dependence.

Applying the Avrami framework, as temperature is increased, one would expect the probability *(p)* of transformation and the growth rate (*G*) of the new phase to both increase. An increase in these parameters will increase the rate constant (Equation 13). However, when the experimental data are normalized per characteristic time, the data at the two temperatures do not converge (Figure S16). This suggests the difference between 77 and 87 K cannot be attributed solely to an increased rate constant.

At 77 K, the fitted N_2 shape parameters are close to 1.5, consistent with diffusion-limited nucleation of a new phase (Equations 12-AD, 16). At 87 K, the N_2 shape parameters are close to unity, consistent with one or more of the following: (a) the semi-empirical LDF equation and statistical aberrations, (b) one-dimensional heterogeneous phase growth (Equation 12-B), or (c) linear condensation in a single annulus with a decreasing inner diameter (Equation 15). The latter two suggest linear phase growth at 87 K and cannot be explained by a growth rate that is limited by diffusion. Thus, the shape parameters suggest "reaction" (or phase-transition) control at 87 K, whereas it was "diffusion" controlled at 77 K. As the GO phase transition is accompanied by a sharp increase in lattice spacing, the diffusional control is exacerbated by a lack of opening. The effects of growth rate and probability on the rate of transformation become much more pronounced when the growth rate is proportion to square root of time (i.e. Equation 12-AD). Thus diffusion control at 77 K amplify the influence of the probability and growth rate on the shape of the rate curves.

We also note that it is not uncommon for the Avrami shape parameter to vary with temperature. As one example, the crystallization of glass occurred via 1-D surface crystallization (λ=1) at low temperature and shifted to 3-D bulk crystallization (λ =3) at higher temperatures.[78] We were able to find one example of a shift from the shape parameter to above/below unity (i.e. from the CE to SE), and this was attributed to 'jamming',[76, 79 74] i.e. the transition from a mobile fluid-like state to a solid-like state with restricted motion.[76]

Gas Dependence. There is a strong disparity between the rate curves for the various gases (Figure 5), in terms of both the rate constants and the shape of the curves. H_2 and O_2 have no induction period for adsorption, whereas that of N_2 and Ar are both quite pronounced with sigmoidal behaviour. Notably, similar trends for gas-dependence on the rate of opening are found elsewhere: O_2 and Ar showed logarithmic adsorption rates to Cd(bpndc)(bpy) at 90K, whereas N_2 was sigmoidal[53] (see also Section V, Supporting Information). Qualitatively, this suggests opening is either almost immediate for certain gases, or the smaller gases may adsorb in the closed structure. Within the Avrami framework, the gas dependence is captured in the dependence of the probability of transformation on the chemical dependence (Equation 6).

It is unclear whether H_2 opens the structure due to its low uptake.[21] At both 77 and 87 K, the H_2 shape parameter is close to that determined empirically for Fickian diffusion (i.e. 0.65 from Ref.[36]), and even closer to that expected from diffusion-limited growth of a new condensed adsorbed phase in a rigid host (i.e. ~0.5, Equations 14, 16).

The high uptake of oxygen suggests it does open the structure, and its rapid rate constant suggests it is relatively unimpeded to diffuse within the structure. The O_2 shape parameter exceeds unity (Table 1), inconsistent with a process that can be solely attributed to adsorption. Yet, a single mechanistic regime is observed in the Avrami plots (Figures 4A" and 4B", Table 1), which seems to suggest the opening process is unimpeded by oxygen diffusivity and/or diffusivity and opening occur simultaneously. Thus, the probability for phase transition for oxygen is high, due either to a high chemical potential for opening[‡‡] and/or a high diffusivity to maximize the probability of opening.

In contrast, both N_2 and Ar have a pronounced induction period at 77 K (Figure 5A). Two-regimes are noted for N_2 and Ar in the super-log Avrami plots (Figure 5A"), suggesting two mechanistic regimes. Shape parameters from the linear fits are summarized in Table 2. The shift occurs at low coverage: ~2% for N_2 and ~1% for Ar at 77 K and 90 mbar. In the first phase, a shape parameter below unity is consistent with diffusion-limited phase growth into a single region (Equations 14, 16). After ~1 hour (~2.5 hours for Ar), a shape parameter of ~1.5 implies the regions begin to impinge (Equations 16, 18). Compared to O_2, the two regimes seem to imply that the larger N_2 and Ar molecules diffuse into the structure prior to opening it. It seems likely that the amount of the larger gas that diffuses into the structure at short time is insufficient to open it. This would imply the gas with the increased diffusivity would have a decreased induction time.

Summary and Conclusions

Transport of gases in flexible gate opening metal-organic frameworks (GO-MOFs) is influenced by both relaxation and diffusion, particularly at low temperatures. Severe mass transfer limitations complicate interpretation of adsorption isotherms and lead to error in interpretation. Significant adsorption may occur at pressures at or below the P_{GO}, given a sufficient induction period. At 77K, sigmoidal adsorption rate curves are observed for N_2 and Ar, but not for H_2 or O_2. At 87 K, the induction period for these four gases is minimal. Analysis of the rate data suggests reaction and diffusion occur over similar time scales, and reaction-diffusion models that incorporate the pseudo-steady state approximation cannot adequately describe the 77K adsorption data.

To describe adsorption kinetics, a somewhat empirical stretched exponential function is commonly applied, with the shape parameter expected to be less than or equal to unity. Conversely, a compressed exponential function is commonly applied to describe the kinetics of phase transitions, with the shape parameter greater than or equal to unity. Our experimental data bracket these two regimes.

Here, we reapply Avrami's theory for the kinetics of phase transition to adsorption, treating adsorption as a phase transition from the "no gas" to "adsorbed film" phases, with or without opening. The resulting equations lead to a shape parameter below unity when adsorption occurs to the particle exterior. The shape parameter exceeds unity when adsorption (with or without opening) is dispersed throughout the particle. Dispersion of nucleation sites can be qualitatively related to the probability of opening, as influenced by diffusion. This generalized Avrami theory is able to qualitatively explain the somewhat anomalous adsorption rate data to RPM3-Zn, including trends with temperature, pressure, and adsorbate, including a somewhat abrupt gas-dependent shift in mechanism with a 10 K temperature change.

Acknowledgements

Original isotherm data was supported by the U.S. Department of Energy, Energy Efficiency and Renewable Energy program, Award DE-FG36-08GO18139. The rate data was collected with support from the U.S. Department of Energy, Basic Energy Sciences, Single Investigator and Small-Group Research (SISGR) program, Awards DE-FG02-09ER466556 and DE-SC0002157. AL thanks Mark Thomas and Milton Cole for discussions of adsorption rate models; Scott Milner, Fawzi Hamad, and Ralph Colby for discussions of Avrami kinetics.

Notes and references

‡ Current Address: Feng Chia University, Taiwan
§ Current Address: Intel Corporation, Hillsboro, Oregon

[‡‡] Using the Clausius-Clapeyron equation, the heats of adsorption for O_2 is estimated to be 12 kJ/mol, versus 8 kJ/mol for N_2, thus verifying the oxygen chemical potential is higher than that of N_2.

§§ This data was collected manually on volumetric adsorption equipment and lacked sufficient resolution at short time.

§§§ This data had only one observed regime.

1. G. Férey, *Chem. Soc. Rev.*, 2008, **37**, 191-214.
2. R. Kitaura, K. Seki, G. Akiyama and S. Kitagawa, *Angew. Chem. Int. Ed.*, 2003, **42**, 428.
3. F. X. Coudert, A. Boutin and A. H. Fuchs, *Mol. Phys.*, 2014, **112**, 1257-1261.
4. F. X. Coudert, A. Boutin, A. H. Fuchs and A. V. Neimark, *J. Phys. Chem. Lett.*, 2013, **4**, 3198-3205.
5. F. X. Coudert, A. Boutin, M. Jeffroy, C. Mellot-Draznieks and A. H. Fuchs, *Chemphyschem*, 2011, **12**, 247-258.
6. A. V. Neimark, F.-X. Coudert, A. Boutin and A. H. Fuchs, *J. Phys. Chem. Lett.*, 2009, **1**, 445-449.
7. F. X. Coudert, M. Jeffroy, A. H. Fuchs, A. Boutin and C. Mellot-Draznieks, *J. Am. Chem. Soc.*, 2008, **130**, 14294-14302.
8. H. Sugiyama, S. Watanabe, H. Tanaka and M. T. Miyahara, *Langmuir*, 2012, **28**, 5093-5100.
9. S. Watanabe, H. Sugiyama, H. Adachi, H. Tanaka and M. T. Miyahara, *J. Chem. Phys.*, 2009, **130**, 164707.
10. P. Mishra, S. Edubilli, H. P. Uppara, B. Mandal and S. Gumma, *Langmuir*, 2013, **29**, 12162-12167.
11. A. Kondo, H. Noguchi, S. Ohnishi, H. Kajiro, A. Tohdoh, Y. Hattori, W. C. Xu, H. Tanaka, H. Kanoh and K. Kaneko, *Nano Lett.*, 2006, **6**, 2581-2584.
12. C. Serre, F. Millange, C. Thouvenot, M. Nogues, G. Marsolier, D. Louer and G. Ferey, *J. Am. Chem. Soc.*, 2002, **124**, 13519-13526.
13. G. Ferey, M. Latroche, C. Serre, F. Millange, T. Loiseau and A. Percheron-Guegan, *Chem. Commun.*, 2003, **24**, 2976-2977.
14. N. Nijem, H. Wu, P. Canepa, A. Marti, K. J. Balkus, Jr., T. Thonhauser, J. Li and Y. J. Chabal, *J. Am. Chem. Soc.*, 2012, **134**, 15201-15204.
15. Y. Kubota, M. Takata, R. Matsuda, R. Kitaura, S. Kitagawa and T. C. Kobayashi, *Angew. Chem. Int. Edit.*, 2006, **45**, 4932-4936.
16. A. Kondo, H. Noguchi, L. Carlucci, D. M. Proserpio, G. Ciani, H. Kajiro, T. Ohba, H. Kanoh and K. Kaneko, *J. Am. Chem. Soc.*, 2007, **129**, 12362-12363.
17. F. X. Coudert, A. U. Ortiz, V. Haigis, D. Bousquet, A. H. Fuchs, A. Ballandras, G. Weber, I. Bezverkhyy, N. Geolfroy, J. P. Bellat, G. Ortiz, G. Chaplais, J. Patarin and A. Boutin, *J. Phys. Chem. C*, 2014, **118**, 5397-5405.
18. H. Sato, W. Kosaka, R. Matsuda, A. Hori, Y. Hijikata, R. V. Belosludov, S. Sakaki, M. Takata and S. Kitagawa, *Science*, 2014, **343**, 167-170.
19. M. Kondo, S. Furukawa, K. Hirai, T. Tsuruoka, J. Reboul, H. Uehara, S. Diring, Y. Sakata, O. Sakata and S. Kitagawa, *J. Am. Chem. Soc.*, 2014, **136**, 4938-4944.
20. A. J. Lan, K. H. Li, H. H. Wu, L. Z. Kong, N. Nijem, D. H. Olson, T. J. Emge, Y. J. Chabal, D. C. Langreth, M. C. Hong and J. Li, *Inorg. Chem.*, 2009, **48**, 7165-7173.
21. S. Sircar, H. Wu, J. Li and A. D. Lueking, *Langmuir*, 2011, **27**, 14169-14179.
22. E. L. Cussler, *Diffusion Mass Transfer in Fluid Systems*, Cambridge University Press, New York, 1997.
23. J. R. Xiao and J. Wei, *Chem. Eng. Sci.*, 1992, **47**, 1123-1141.
24. A. I. Skoulidas and D. S. Sholl, *J. Phys. Chem. B*, 2005, **109**, 15760-15768.
25. J. Liu, J. Y. Lee, L. Pan, R. T. Obermyer, S. Simizu, B. Zande, S. G. Sankar, J. Li and J. K. Johnson, *Mol. Simulat.*, 2011, **37**, 640-646.
26. A. J. Fletcher, E. J. Cussen, D. Bradshaw, M. J. Rosseinsky and K. M. Thomas, *J. Am. Chem. Soc.*, 2004, **126**, 9750-9759.
27. A. J. Fletcher, E. J. Cussen, T. J. Prior, M. J. Rosseinsky, C. J. Kepert and K. M. Thomas, *J. Am. Chem. Soc.*, 2001, **123**, 10001-10011.
28. A. J. Fletcher and K. M. Thomas, *Langmuir*, 2000, **16**, 6253-6266.
29. D. S. Sholl and K. A. Fichthorn, *Phys. Rev. Lett.*, 1997, **79**, 3569-3572.
30. L. Sarkisov, T. Düren and R. Q. Snurr, *Molec. Phys.*, 2004, **102**, 211-221.
31. Z. B. Bao, L. A. Yu, Q. L. Ren, X. Y. Lu and S. G. Deng, *J. Colloid Interf. Sci.*, 2011, **353**, 549-556.

32. C. R. Reid and K. M. Thomas, *Langmuir*, 1999, **15**, 3206-3218.
33. J. Crank, *The mathematics of diffusion*, Oxford university press, 1979.
34. S. Sircar and J. R. Hufton, *Adsorption*, 2000, **6**, 137-147.
35. R. M. Rynders, M. B. Rao and S. Sircar, *Aiche J*, 1997, **43**, 2456-2470.
36. L. Li, J. G. Bell, S. Tang, X. Lv, C. Wang, Y. Xing, X. Zhao and K. M. Thomas, *Chem Mater*, 2014, **26**, 4679-4695.
37. K. F. Loughlin, M. M. Hassan, A. I. Fatehi and M. Zahur, *Gas Sep Purif*, 1993, **7**, 264-273.
38. D. M. Ruthven, N. S. Raghavan and M. M. Hassan, *Chem. Eng. Sci.*, 1986, **41**, 1325-1332.
39. F. R. Fitch, M. Bulow and A. I. Lacava, *Gas Sep Purif*, 1994, **8**, 45-51.
40. H. K. Chagger, F. E. Ndaji, M. L. Sykes and K. M. Thomas, *Carbon*, 1995, **33**, 1405-1411.
41. G. Astarita and L. Nicolais, *Pure Appl. Chem.*, 1983, **55**, 727-736.
42. C. M. Hansen, *Eur Polym J*, 2010, **46**, 651-662.
43. A. J. Fletcher, Y. Uygur and K. M. Thomas, *J. Phys. Chem. C*, 2007, **111**, 8349-8359.
44. M. Švábová, Z. Weishauptová and O. Přibyl, *Fuel*, 2011, **90**, 1892-1899.
45. X. Zhao, S. Villar-Rodil, A. J. Fletcher and K. M. Thomas, *J. Phys. Chem. B*, 2006, **110**, 9947-9955.
46. X. Y. Xia and P. G. Wolynes, *Phys. Rev. Lett.*, 2001, **86**, 5526-5529.
47. D. Apitz and P. M. Johansen, *J. Appl. Phys.*, 2005, **97**, 063507-063504.
48. P. K. Gupta and J. C. Mauro, *Phys. Rev. E*, 2008, **78**, 062501.
49. M. D. Ediger, C. A. Angell and S. R. Nagel, *J. Phys. Chem.*, 1996, **100**, 13200-13212.
50. G. Williams and D. C. Watts, *Trans. Faraday Soc.*, 1970, **66**, 80-&.
51. J. Klafter and A. Blumen, *Chem. Phys. Lett.*, 1985, **119**, 377-382.
52. E. W. Hansen, X. L. Gong and Q. Chen, *Macromol. Chem. Phys.*, 2013, **214**, 844-852.
53. D. Tanaka, K. Nakagawa, M. Higuchi, S. Horike, Y. Kubota, L. C. Kobayashi, M. Takata and S. Kitagawa, *Angew. Chem. Int. Edit.*, 2008, **47**, 3914-3918.
54. O. Levenspiel, *Chemical reaction engineering*, Wiley New York etc., 1972.
55. N. J. Kuipers and A. A. Beenackers, *Polym. Eng. Sci.*, 1996, **36**, 2108-2118.
56. N. J. M. Kuipers and A. A. C. M. Beenackers, *Chem. Eng. Sci.*, 1993, **48**, 2957-2971.
57. C. R. Reid, I. P. O'Koy and K. M. Thomas, *Langmuir*, 1998, **14**, 2415-2425.
58. K. Malek and M.-O. Coppens, *J. Chem. Phys.*, 2003, **119**, 2801-2811.
59. H. L. Frisch, *Polym. Eng. Sci.*, 1980, **20**, 2-13.
60. N. A. Peppas and J. L. Sinclair, *Colloid Polym. Sci.*, 1983, **261**, 404-408.
61. M. Olinick, *An Introduction to Mathematical Models in the Social and Life Sciences*, Addison-Wesley, Reading, MA, 1978.
62. R. Gutierrez-Jaimez, P. Roman, D. Romero, J. J. Serrano and F. Torres, *Math. Biosci.*, 2007, **208**, 147-165.
63. C. P. D. Birch, *Annals Bot.-London*, 1999, **83**, 713-723.
64. I. D. Bassukas, *Cancer Res.*, 1994, **54**, 4385-4392.
65. M. Avrami, *J. Chem. Phys.*, 1939, **7**, 1103-1112.
66. M. Avrami, *J. Chem. Phys.*, 1940, **8**, 212-224.
67. P. Jain, D. A. Fonseca, E. Schaible and A. D. Lueking, *J. Phys. Chem. C*, 2007, **111**, 1788-1800.
68. S. Sircar and A. D. Lueking, PhD Thesis, The Pennsylvania State University, 2014.
69. S. Sircar, S. Pramanik, J. Li, M. W. Cole and A. D. Lueking, *J. Colloid Interface Science*, 2015, **446**, 177-184.
70. H. Y. Kim, A. D. Lueking, S. M. Gatica, J. K. Johnson and M. W. Cole, *Mol. Phys.*, 2008, **106**, 1579-1585.
71. J. G. Jee, M. B. Kim and C. H. Lee, *Chem. Eng. Sci.*, 2005, **60**, 869-882.
72. T. J. Giesy and M. D. LeVan, *Chem. Eng. Sci.*, 2013, **90**, 250-257.
73. S. V. Mazumder, F.; Bruining, J, *Soc. Petrol. Eng. J.*, 2011, **16**, 856-863.
74. L. Cipelletti, L. Ramos, S. Manley, E. Pitard, D. A. Weitz, E. E. Pashkovski and M. Johansson, *Faraday Discuss*, 2003, **123**, 237-251.
75. L. Cipelletti, S. Manley, R. C. Ball and D. A. Weitz, *Phys. Rev. Lett.*, 2000, **84**, 2275-2278.
76. P. Falus, S. Narayanan, A. R. Sandy and S. G. J. Mochrie, *Phys. Rev. Lett.*, 2006, **97**, 066102.
77. R. Bandyopadhyay, D. Liang, H. Yardimci, D. A. Sessoms, M. A. Borthwick, S. G. J. Mochrie, J. L. Harden and R. L. Leheny, *Phys. Rev. Lett.*, 2004, **93**, 228302.
78. M. Romero, R. D. Rawlings and J. M. Rincon, *J. Eur. Ceram. Soc.*, 1999, **19**, 2049-2058.
79. M. E. Cates, J. P. Wittmer, J. P. Bouchaud and P. Claudin, *Phys. Rev. Lett.*, 1998, **81**, 1841-1844.

Journal Name

ARTICLE

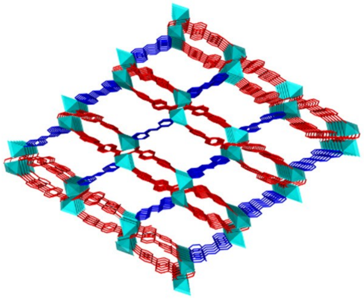

Fig. 1 The structure of RPM3-Zn. Zn atoms (cyan) coordinate to carboxylate groups of bpdc (red) to form 2D brick-like nets. The pillar ligand bpee (blue) bonds to the metals in the adjacent nets to complete the tetrahedral geometry of Zn atoms, giving rise to the overall 3D structure. The framework is porous, containing 1D open channel along the b axis with pore dimension of ~ 5 X 7 Å.

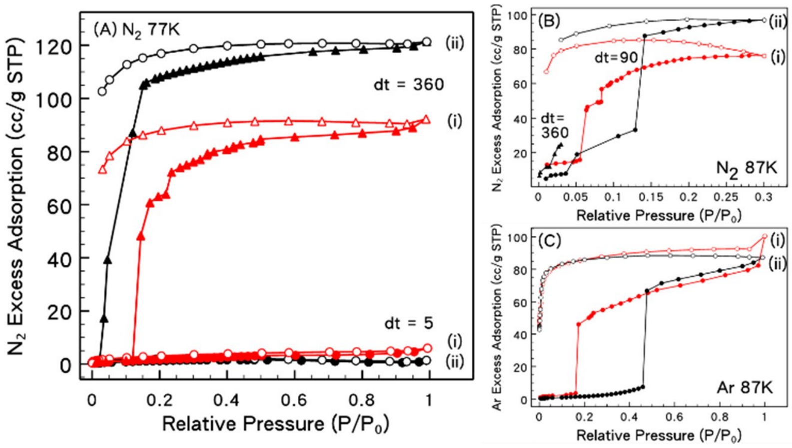

Fig. 2 RPM3-Zn adsorption isotherms for (a) N_2 at 77 K, (b) 87K, and (c) Ar at 87K (i in red, ii in black). The frequency of automated pressure stability checks (dt) was manipulated to lengthen the total time of data collection for each isotherm point, and this significantly altered the shape of the adsorption isotherm, as discussed previously [21]. The (dt) of (c) is 5 seconds. Subsequent kinetic data is normalized per the PGOs estimated from these isotherms, at the pressure at which the jump started to occur: For i, PGO/Po is estimated to be (a) 0.14, (b) 0.06, (c) 0.16; For ii, PGO/Po is ~ (a) 0.03, (b) 0.04, 0.47

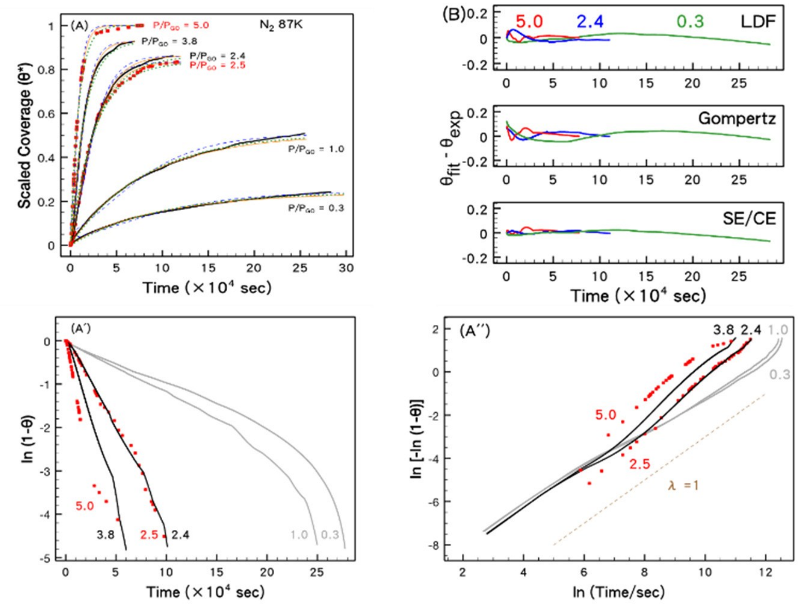

Fig. 3 (A) Adsorption rates, model fits, and (B) model fitting residuals (select) for N$_2$ adsorption to RPM3-Zn at 77K (i, symbols; ii, solid lines). Select model fits include LDF/DE/SE (green, dotted lines), CE (orange, solid lines), and Gompertz (blue, dashed lines). Data fits of the DE and SE were indistinguishable from the LDF. Data annotations refer to P/PGO, with absolute pressures of 220 mbar for i, and (from left to right) of 223, 91, 43, 23 mbar for ii. Data for (A) is scaled to the maximum capacity at the highest pressure to show the relative magnitudes at the different pressures. Data is then transformed to (A') semi-log and (A") super log-log plots, in line with the LDF (A') and SE/CE (A") equations. Additional transformations are included in the Supporting Information.

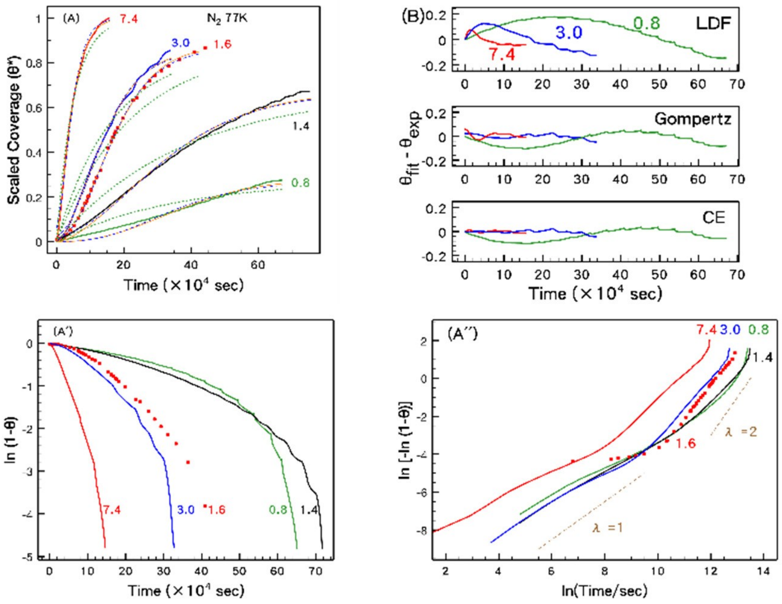

Fig. 4 (A) Adsorption rates, model fits, and (B) model fitting residuals for N$_2$ adsorption to RPM3-Zn at 87K for i (red squares) and ii (black lines). Pressures are 829 mbar (P/PGO = 5.0) and 414 mbar (P/PGO = 2.5) for i; 414 mbar (P/PGO = 3.8), 265 mbar (P/PGO = 2.4), 106 mbar (P/PGO = 1.0), 30.0 mbar (P/PGO = 0.3) for ii. Data in (A) is scaled to the maximum capacity to show the relative magnitudes at the different pressures. The legend for the various models and transformations are defined in Figure 3. Data fits of the DE and SE were indistinguishable from the LDF.

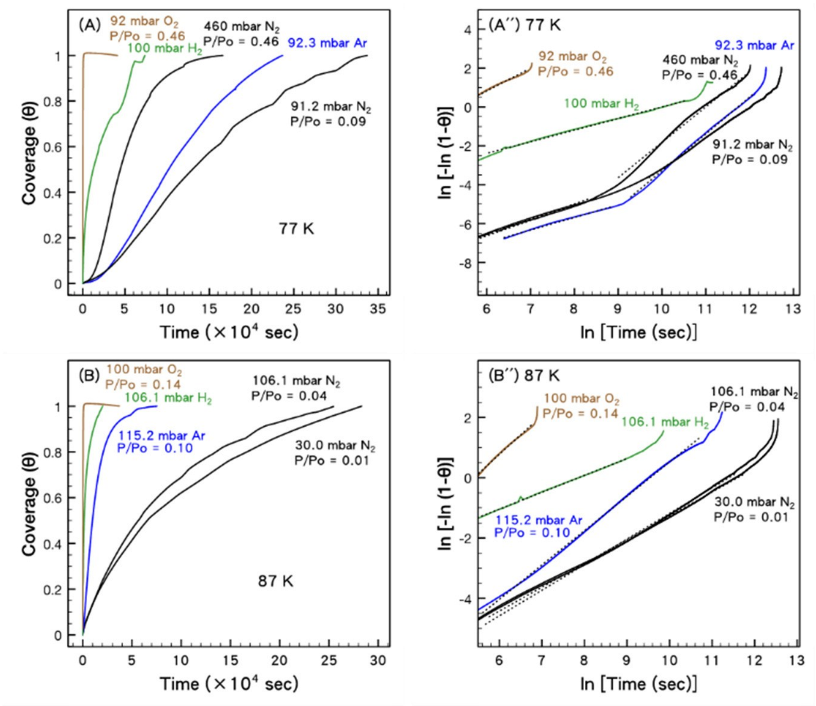

Fig. 5 Adsorption rate curves for various gases to RPM3-Zn at (A) 77K and (B) 87 K. The N_2 rate data is reproduced from Figures 3 and 4, including the super-log log transformation according to the SE/CE models; additional transformations can be found in the Supporting Information.

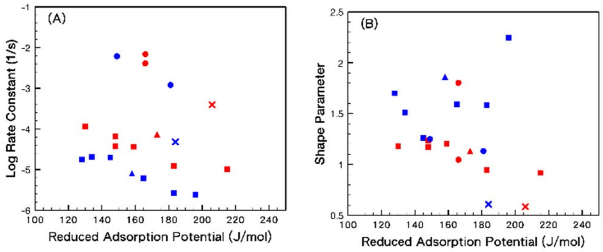

Fig. 6 Summary of Fitted Rate Parameters for the SE/CE kinetic expression, for N_2 (■), O_2 (●), Ar (▲), and H_2 (X) at 77 K (blue) and 87 K (red). The reduced adsorption potential is the chemical potential normalized by the critical properties, i.e. - RT/TC ln (P/PC), as discussed elsewhere.[69] Thus, pressure increases to the left. The adsorption potential of H_2 has arbitrarily been divided by 10 to plot it on the same figure.

Table 1: Data fits of the full experimental data to the SE/CE model. The shape parameter, λ, was allowed to vary. Additional fitting statistics for other models are found in the Supporting Information.

Gas_T(K)_P(mbar)	Rate Constant k (s^{-1})	Shape Parameter λ (Full Data Fit)	R^2	Two-regime λ (Avrami Plots)
N2_77_23	2.40×10^{-6}	2.24	0.9976	0.7, 1.9
N2_77_43	2.67×10^{-6}	1.58	0.9987	0.8, 1.5
N2_77_220	5.07×10^{-6}	1.77	0.9997	$1.8^{\S\S}$
N2_77_91	6.11×10^{-6}	1.59	0.9997	0.8, 1.6
N2_77_223	1.99×10^{-5}	1.26	0.9999	0.7, 1.3
N2_77_355	2.03×10^{-5}	1.51	0.9999	0.5, 1.6
N2_77_460	1.75×10^{-5}	1.70	0.9995	0.8, 1.8
N2_87_30	1.02×10^{-5}	0.917	0.9989	$0.8^{\S\S\S}$
N2_87_106	1.22×10^{-5}	0.947	0.9997	$0.9^{\S\S\S}$
N2_87_265	3.66×10^{-5}	1.21	0.9998	0.9, 1.2
N2_87_414	3.78×10^{-5}	1.17	0.9995	$1.3^{\S\S}$
N2_87_414	6.52×10^{-5}	1.24	0.9997	0.9, 1.2
N2_87_829	1.15×10^{-4}	1.18	0.9998	$1.3^{\S\S}$
Ar_77_92	8.07×10^{-6}	1.86	0.9996	0.6, 1.9
Ar_87_115	7.31×10^{-5}	1.13	0.9998	$1.1^{\S\S\S}$
O2_77_92	6.12×10^{-3}	1.25	0.9998	$1.2^{\S\S\S}$
O2_87_100	6.88×10^{-3}	1.05	1.00	$1.3^{\S\S\S}$
H2_77_100	4.83×10^{-5}	0.607	0.9969	$0.60^{\S\S\S}$
H2_87_106	3.92×10^{-4}	0.584	0.9996	$0.56^{\S\S\S}$

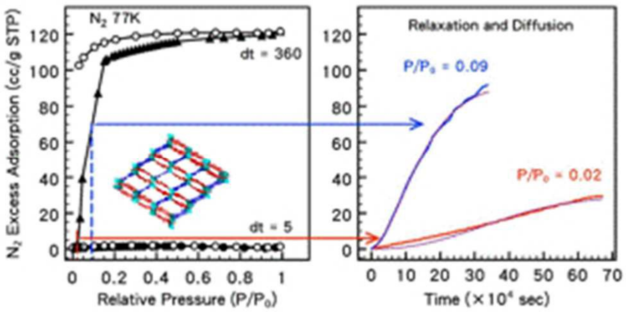

111x55mm (72 x 72 DPI)